ACS central science

http://pubs.acs.org/journal/acscii

Research Article

Riemannian Surface on Carbon Anodes Enables Li-Ion Storage at −35 °C

Zongjing Lu,[#] Jingnan Wang,[#] Xuechun Cheng,[#] Weiwei Xie, Zhiyi Gao, Xuejing Zhang, Yong Xu, Ding Yi, Yijun Yang, Xi Wang,* and Jiannian Yao*

Cite This: https://doi.org/10.1021/acscentsci.2c00411

Read Online

ACCESS | Metrics & More | Article Recommendations | Supporting Information

ABSTRACT: Since sluggish Li^+ desolvation leads to severe capacity degradation of carbon anodes at subzero temperatures, it is urgently desired to modulate electron configurations of surface carbon atoms toward high capacity for Li-ion batteries. Herein, a carbon-based anode material (O-DF) was strategically synthesized to construct the Riemannian surface with a positive curvature, which exhibits a high reversible capacity of 624 mAh g^{-1} with an 85.9% capacity retention at 0.1 A g^{-1} as the temperature drops to −20 °C. Even if the temperature drops to −35 °C, the reversible capacity is still effectively retained at 160 mAh g^{-1} after 200 cycles. Various characterizations and theoretical calculations reveal that the Riemannian surface effectively tunes the low-temperature sluggish Li^+ desolvation of the interfacial chemistry via locally accumulated charges of non-coplanar sp^x ($2 < x < 3$) hybridized orbitals to reduce the rate-determining step of the energy barrier for the charge-transfer process. Ex-situ measurements further confirm that the sp^x-hybridized orbitals of the pentagonal defect sites should denote more negative charges to solvated Li^+ adsorbed on the Riemannian surface to form stronger Li−C coordinate bonds for Li^+ desolvation, which not only enhances Li-adsorption on the curved surface but also results in more Li^+ insertion in an extremely cold environment.

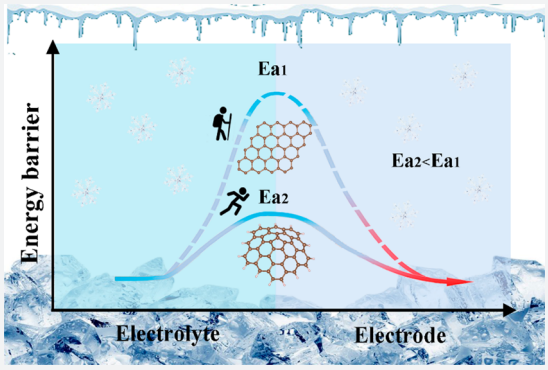

INTRODUCTION

Lithium-ion batteries (LIBs) have been universally applied in various portable electronics and electric vehicles due to a high energy density and long cycle life at room temperature,[1,2] but they still suffer from poor performance at subzero temperatures, especially substantial energy and power losses, which severely limits their operations in a cold environment such as high-altitude areas and aerospace explorations as well as electric vehicles under extreme conditions.[3−6] This issue has attracted more attention from the scientific and industrial communities.

Up to now, various strategies have primarily focused on electrolytes and electrodes to solve the above issue via the tailoring of electrolyte structures and the introduction of electrolyte additives to reduce the freezing point and boost ionic conductivity,[1−3,7,8] or the surface modification of the electrode structure to lower the charge-transfer energy barrier at the interface.[4,9−11] Most importantly, the consensus reached in recent studies reveals that the dominant reason for the considerable capacity loss at subzero temperatures should be attributed to the high energy barrier of charge-transfer resistance in the sluggish Li^+ desolvation process,[4,12,13] which is closely correlated to the strength of the solvated Li^+ binding energy at the electrolyte−electrode interface.[14,15] On the other hand, graphite with a theoretical capacity of 372 mAh g^{-1}, as commercial state-of-the-art anodes for LIBs, endures severe capacity degradation as the temperature declines,[16,17] of which its capacity rapidly decays to only 12 mAh g^{-1} at −20 °C.[10,18] These results apparently indicate that the solvated Li^+ binding to sp^2 hybridized carbon sites with a conjugated π-electron system is too weak to get rid of the solvation sheath for Li^+ desolvation before the intercalation of naked Li^+ into graphite interlayers and overcome the rate-determining step of energy barrier for the charge-transfer process, which may be the essential hindrances for the low-temperature operation of LIBs.[19] Therefore, the key to addressing the low-temperature capacity loss lies in adjusting the surface electron configurations of the carbon anode to reinforce the coordinate interaction between the solvated Li^+ and adsorption sites for Li^+ desolvation and reduce the activation energy of the charge-transfer process. In addition, with inspiration from the geometric architectures of carbon allotropes with positive and negative curvatures, it is expected to manipulate the

Received: April 7, 2022

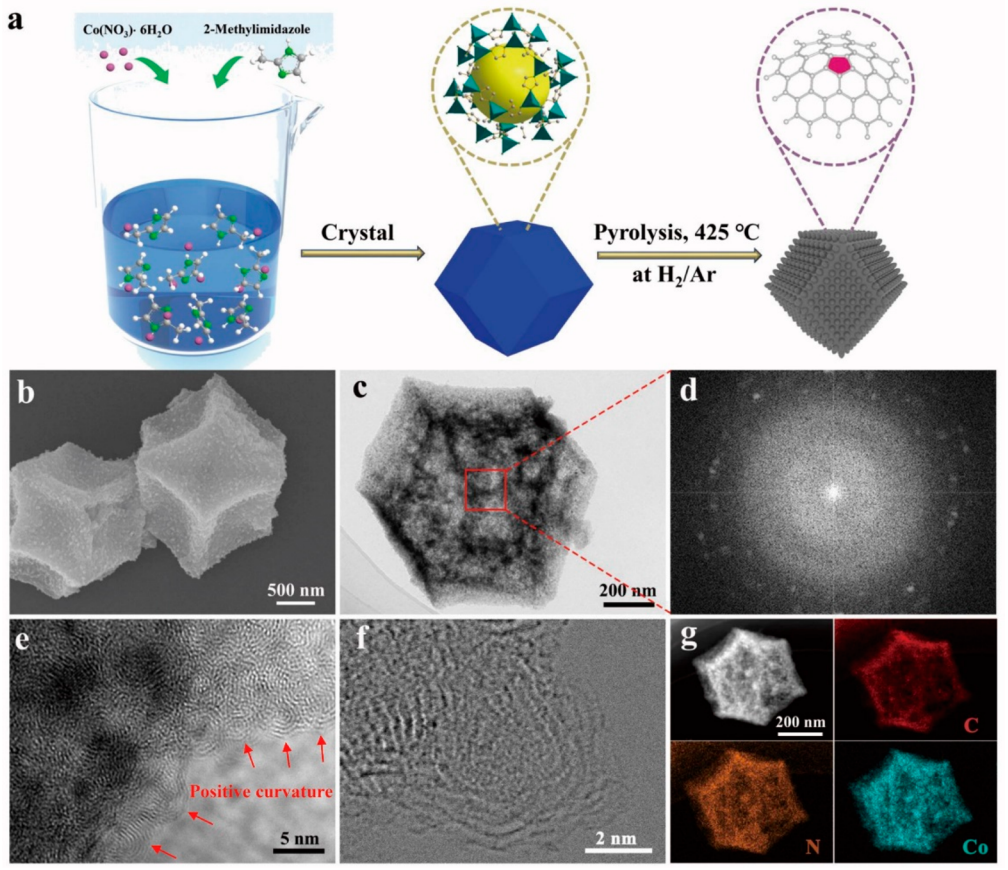

Figure 1. (a) Schematic illustration of the synthesis process of O-DF. (b–d) SEM, TEM, and the corresponding SAED images of O-DF. (e, f) HRTEM images of O-DF with different magnifications. (g) Elemental mappings of C, N, and Co for O-DF.

electronic configurations of the surface through the transformation of hybridized orbital types generated by the response of chemical bonds to bending deformations,[20−22] where the insertion of one pentagon into an sp^2-hybridized hexagon lattice generates a surface with a positive curvature like a bowl, while the introduction of one heptagon or larger membered rings produces a surface with a negative curvature like a saddle.[23,24] Theoretical calculations demonstrate that the curved surfaces bind lithium with a stronger affinity than the planar surface with zero curvature, particularly the structure with a positive curvature (Figure S1), making it possible to accomplish the high capacity of the carbon anode in an extremely cold environment. However, the carbon anode with a positive curvature as a high capacity electrode material for Li-ion storage at low temperature has never been realized, and the underlying structure-performance relation has not been theoretically and experimentally uncovered.

Herein, we strategically prepared multilayer onion-like carbon nanospheres anchored on the dodecahedral carbon framework (O-DF) through direct low-temperature pyrolysis of zeolitic imidazolate framework-67 (ZIF-67), which possesses a non-coplanar Riemann surface with a positive curvature. When the temperature declines to −20 °C, the O-DF carbon-based anode for LIBs exhibits a high reversible capacity of 624 mAh g^{-1} with an 85.9% capacity retention at 0.1 A g^{-1}, far surpassing the commercial state-of-the-art graphite with zero curvature. Even if the temperature drops to −35 °C, O-DF is still effectively retained at the reversible capacity of 160 mAh g^{-1} at 0.1 A g^{-1} after 200 cycles. Combining the physical characterizations with theoretical calculations, we found that the carbon atoms with unsaturated coordination among the pentagonal defects embedded into the Riemann surface tend to adopt new-typed non-coplanar sp^x ($2 < x < 3$) hybridization, which breaks the conjugated π-electron system of sp^2-hybridized orbitals and motivates the local charge accumulation. The sp^x-hybridized orbitals facilitate charge donation to strengthen Li−C coordinate bonds for Li^+ desolvation to reduce the activation energy of the charge-transfer process, which not only enhances the Li-adsorption on the curved surface but also results in more Li^+ insertion in an extremely cold environment.

RESULTS AND DISCUSSION

To ingeniously implement the positively curved surface design of carbon anodes, ZIF-67 precursors composed of pentagonal structures as basic units provide the possibility for inducing a large number of pentagonal defects embedded into the planar sp^2 hexagonal lattice with appropriate pyrolysis conditions. As illustrated in Figure 1a, through direct pyrolysis of ZIF-67 containing Co, C, and N atoms at 425 °C under a 10% H_2/Ar atmosphere, O-DF was first synthesized to construct the local surface with positive curvature.

The synthesis mechanism of O-DF is shown in the Supporting Information. Thermogravimetric analysis (TGA) affirms that, by controlling the decomposition temperature at 425 °C, it ensures that one partial 2-methylimidazole proceeds to the decomposition behavior, and the other retains five-membered ring structures (Figure S2). It is noteworthy to

https://doi.org/10.1021/acscentsci.2c00411
ACS Cent. Sci. XXXX, XXX, XXX−XXX

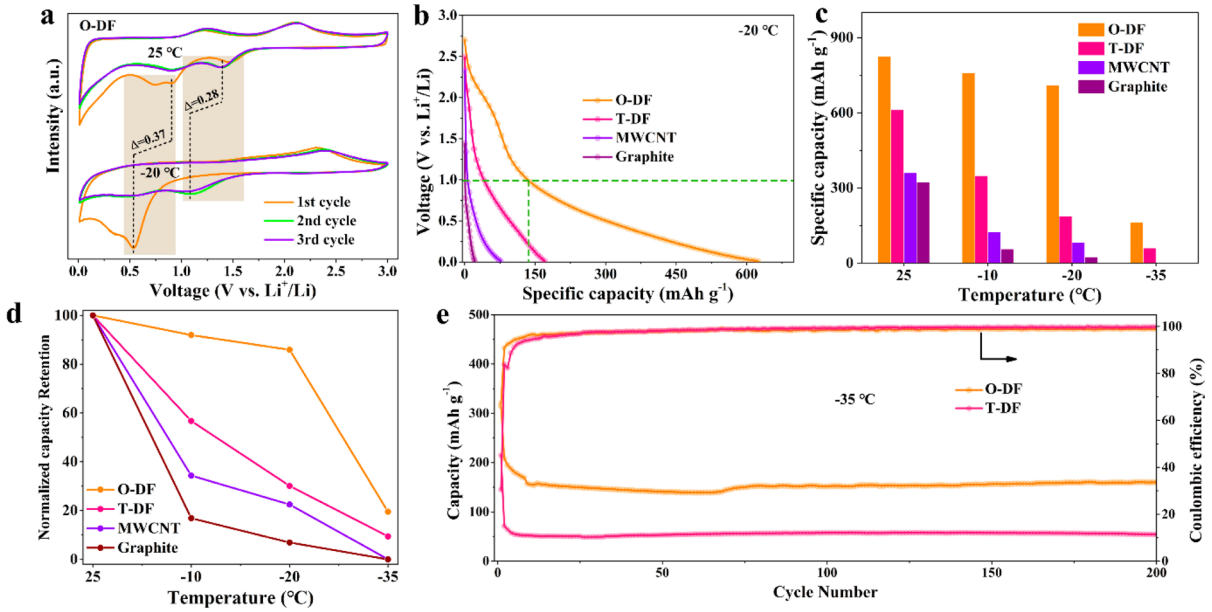

Figure 2. (a) CV curves of O-DF for −20 °C at 0.1 mV s^{-1} compared with the corresponding curves for room temperature. (b) Galvanostatic discharge curves of O-DF, T-DF, MWCNT, and graphite for −20 °C at 0.1 A g^{-1} after 150 cycles. (c, d) Cyclic capacity comparisons (c) and normalized capacity retention (d) of O-DF, T-DF, MWCNT, and graphite range from 25 to −35 °C. (e) Long-term cycles and efficiency of O-DF and T-DF for −35 °C at 0.1 A g^{-1}.

mention that 2-methylimidazole serves as not only as a sacrificial template for the growth of the carbon framework but also the source of five-membered ring structures. To the best of our knowledge, the convex spherical surface with a positive curvature, also referred to as the Riemannian surface, has to adopt the insertion of pentagonal defects into a regular hexagon lattice of an sp^2 carbon network to meet the indispensable conditions imposed by Euler's theorem for spherical polyhedrons.[21,24,25] As a comparison with O-DF, N-doped multiwalled carbon nanotubes-interlaced dodecahedron (T-DF) was also prepared using a similar process but only adjusting the pyrolysis temperature to 600 °C (Figure S3).

The scanning electron microscopy (SEM) and transmission electron microscopy (TEM) reveal the morphologic structure of as-synthesized ZIF-67, O-DF, and T-DF (Figure 1 and Figure S4). Even after the thermal treatment, as-obtained O-DF and T-DF with high uniformity still inherit a well-defined dodecahedral framework of the ZIF-67 precursors but exhibit a rough surface (Figure 1b and Figure S4d−i). Obviously, positively curved carbon nanospheres via the inside-out growth are observed all over the external surface of the dodecahedral framework for O-DF (Figure S4f). Different from O-DF with a convex spherical surface, the corresponding surface of T-DF is fully covered with carbon nanofibers due to sufficient pyrolysis (Figure S4i). In contrast to the multistage diffraction rings for T-DF with a relatively high degree of graphitization (Figure S5a), the selective-area electron diffraction (SAED) pattern of O-DF displays a diffuse halo feature (Figure 1c,d), which suggests an amorphous character, originating from abundant carbon intrinsic defects as active sites for Li-ion storage.[26−28]

The high-resolution TEM (HRTEM) images of O-DF further demonstrate the lattice fringes of carbon nanospheres with highly curved fullerene-like multishell structures on edge, less than 6 nm in diameter (Figure 1e,f). Nevertheless, the corresponding lattice fringes of T-DF are not parallel to the axis direction, which show slightly curved graphene-like multiwalled layers, including a convex structure with a positive curvature and a concave structure with a negative curvature (Figure S5), where five-membered rings and seven- or larger membered rings embedding the hexagon lattice of sp^2 carbon network induce the positive curvature and negative curvature, respectively, which belong to the category of non-Euclidean geometry in the field of mathematical research.[21,29−32] As a result, the surface of T-DF with positive and negative curvatures is denoted as non-Euclidean geometric surfaces. Especially, similar to the well-defined Riemannian surface, the concave surface with the negative curvatures is defined in the Lobachevskian surface according to the hyperbolic geometry features. In addition, it is notable that the measured lattice spacings of graphitic layers for O-DF and T-DF display 0.38 and 0.36 nm, respectively, which is slightly larger than the (002) crystal plane of planar graphite (Figure S5b and Figure S6). This result is attributed to the curvature effect, which would be beneficial to the faster diffusion of Li^+ in the bulk phase.[33−35] Obviously, the curved degree of the Riemann surface for O-DF exhibited more prominence than that of the non-Euclidean geometric surface for T-DF. Also, the presence of metallic Co nanoparticles is affirmed. The element mapping images of O-DF show the homogeneous distribution of Co, C, and N elements throughout the dodecahedral structure, manifesting that N atoms are doped into the carbon matrix (Figure 1g).

To evaluate the impact of the atomic-scale Riemann surface and non-Euclidean geometric surface on the electrochemical performances at low temperature, as-synthesized O-DF and T-DF as anode materials for LIBs were investigated by using the CR2025-type coin cells. For reference, commercial multiwalled carbon nanotubes (MWCNTs) and graphite with a typical zero-curvature surface were also tested under identical conditions.

As displayed in Figure 2a and Figure S7, cyclic voltammetry (CV) curves of O-DF and T-DF were measured in the voltage range of 0.01−3.0 V at a scan rate of 0.1 mV s^{-1}. The CV curves of O-DF exhibit an analogical shape regardless of 25 °C

https://doi.org/10.1021/acscentsci.2c00411
ACS Cent. Sci. XXXX, XXX, XXX−XXX

and −20 °C. Concretely, at 25 °C, the distinct reduction peak appears around 0.8 V during the initial cathodic scan but disappears in the following cycles, which could be regarded as the irreversible decomposition of electrolytes to form the solid electrolyte interface (SEI) films.[35] The other reversible reduction peak located at 1.25 V is related to the reduction reaction of cobalt oxide, which may be due to the oxidation of a small number of cobalt nanoparticles on the surface.[36] When the temperature is decreased from 25 °C to −20 °C, the CV curves still remain well-overlapped in subsequent cycles, demonstrating the excellent cycling stability of O-DF. Remarkably, the cathodic peaks at −20 °C present a negative shift, as compared with that at 25 °C, indicating an increase in the electrochemical polarization, which depends on the sluggish interfacial kinetics process at low temperatures. The CV curves of T-DT also show a pattern similar to that of O-DF at the corresponding temperature, while T-DF displays more deteriorated polarization, suggesting that the Riemann surface of O-DF is more conducive to improving the sluggish interfacial kinetics than non-Euclidean geometric surface of T-DF at low temperature.

The galvanostatic discharge (GCD) profiles of O-DF, T-DF, MWCNT, and graphite were further performed for −20 °C at a current density of 0.1 A g^{-1} after 150 cycles, where the discharge specific capacities are 697, 168, 77, and 19 mAh g^{-1}, respectively (Figure 2b). The discharge specific capacities of O-DF are much higher than those of the other three materials. It is noted that the increase in the discharge specific capacity of O-DF is mainly below 1.0 V, indicating that the small amount of cobalt oxide on the surface is not the primary cause of raising the low-temperature capacity.

Moreover, the specific capacities of the four electrodes at different temperatures are compared (Figure 2c and Figure S8). The O-DF anode delivers a remarkable reversible capacity of 823 mAh g^{-1} after 50 cycles at 25 °C, which far surpasses the theoretical capacity of graphite (372 mAh g^{-1}). It can be speculated that the extra capacity of O-DF mainly originates from the Riemann surficial structure with the positive curvature.[21] When the temperature is reduced to −10 °C, the capacity of O-DF is incredulously retained at 756 mAh g^{-1}, which is one of the most prominent low-temperature capacities compared with the previously reported carbon anodes for LIBs. With the temperature further falling to −20 °C, the reversible capacity of 697 mAh g^{-1} could be obtained, far superior to the counterpart of T-DF (184 mAh g^{-1}), whereas MWCNT and graphite lose most of their capacities and nearly fail to operate at this temperature point. Even when the temperature drops to −35 °C, the reversible capacity is still effectively retained at 160 mAh g^{-1} after 200 cycles, which is about three times higher than that of T-DF. Interestingly, to compare the performance well with decreasing temperatures, the capacities were further normalized by the room-temperature value for clarity.[4] As shown in Figure 2d, the capacity retention of O-DF at subzero temperatures was far superior to the other three electrodes, which could impressively deliver an 85.9% capacity retention at −20 °C. In addition, the capacities of O-DF with a Coulombic efficiency of ∼100% hardly decay after the long cycles at the desired temperature until down to −40 °C (Figure 2e and Figure S8), demonstrating the excellent cycle stability and cold tolerance.

Impressively, despite the charge−discharge process being accompanied by the sluggish interfacial kinetics, O-DF still exhibits the highly reversible capacities at each tested low-temperature point. In fact, on the basis of the above-mentioned analysis, the explicit structure distinction among O-DF, T-DF, MWCNT, and graphite lies in the different atomic-scale curved surfaces, including the Riemann surface with a positive curvature, the Lobachevskian surface with a negative curvature, and planar surface with zero curvature. Therefore, it can be speculated that the impressive low-temperature reversible capacities for O-DF should be associated with the typical Riemann surface. However, the intrinsic features of these geometric surfaces have not been thoroughly unveiled, especially the characteristics of the electronic structure, let alone to establish the relation between the structure of the Riemann surface and the low-temperature performance for Li-ion storage.

To identify the structural information of O-DF and T-DF, the physical and chemical structures were characterized. The X-ray diffraction (XRD) patterns and Raman spectra confirm the existence of abundant carbon intrinsic defects and the formation of metallic Co nanoparticles in the dodecahedral frameworks of O-DF and T-DF (Figures S9 and S10), which are in close agreement with the TEM results, as detailed analyses in the Supporting Information. The X-ray photoelectron spectroscopy (XPS) measurements are further carried out to ascertain the differentiation in the chemical states of different curvature structures. In the case of O-DF, the XPS survey spectra reveal the presence of Co, C, N, and O elements (Figure S11a), with the atomic contents of 2.75 atom %, 91.3 atom % (84.41 wt %), 2.88 atom % (3.10 wt %), and 3.07 atom %, respectively. The mass contents of C and N elements tested by elemental analysis are 85.12 and 2.97 wt %, respectively, consistent with the XPS results. The high-resolution Co 2p spectrum of O-DF shows the characteristic peaks of the Co metal at 778.2 (Co $2p^{3/2}$) and 793.5 eV (Co $2p^{1/2}$) (Figure S11b). This result indicates that the Co element of O-DF mainly exists in the form of metallic cobalt nanoparticles, consistent with the TEM and XRD results, illustrating that the coordinate bonds between Co and N atoms are almost completely decomposed during the pyrolysis process of the ZIF- 67 precursor. Generally, the metallic cobalt nanoparticles are expected to effectively enhance the electrical conductivity and accelerate the Li-ion diffusion. Nonetheless, as a consequence of their inertia for lithium storage,[21] it can be determined that these metallic cobalt nanoparticles are impossible as the source of highly reversible capacity at low temperature. Furthermore, the O element should stem from the adsorbed oxygen from the air.[18] The high-resolution XPS N 1s spectrum can be deconvoluted into three peaks located at 398.4, 399.8, and 401.2 eV, corresponding to pyridinic-N, pyrrolic-N, and graphitic-N, respectively (Figure S11c).[12,19] Apparently, the trace and similar nitrogen contents not only fail to explain the source of the extra capacity but also are irrelevant to the distinct capacities between O-DF and T-DF at the identical temperature (Table S1), although these nitrogen species could partly regulate the electronic structures and serve as the active sites for Li-ion storage.[17,19] In addition, the specific surface area of O-DF is distinctly less than the counterpart of T-DF (Figure S12), as detailed analyses in the Supporting Information. These results confirm that the different surface intrinsic carbon defects may cause the variance in the low-temperature capacity for O-DF and T-DF.

To further explore the source of the highly reversible capacity and reveal the structure−capacity correlation at low temperature, the distinction of intrinsic carbon defects with

https://doi.org/10.1021/acscentsci.2c00411
ACS Cent. Sci. XXXX, XXX, XXX−XXX

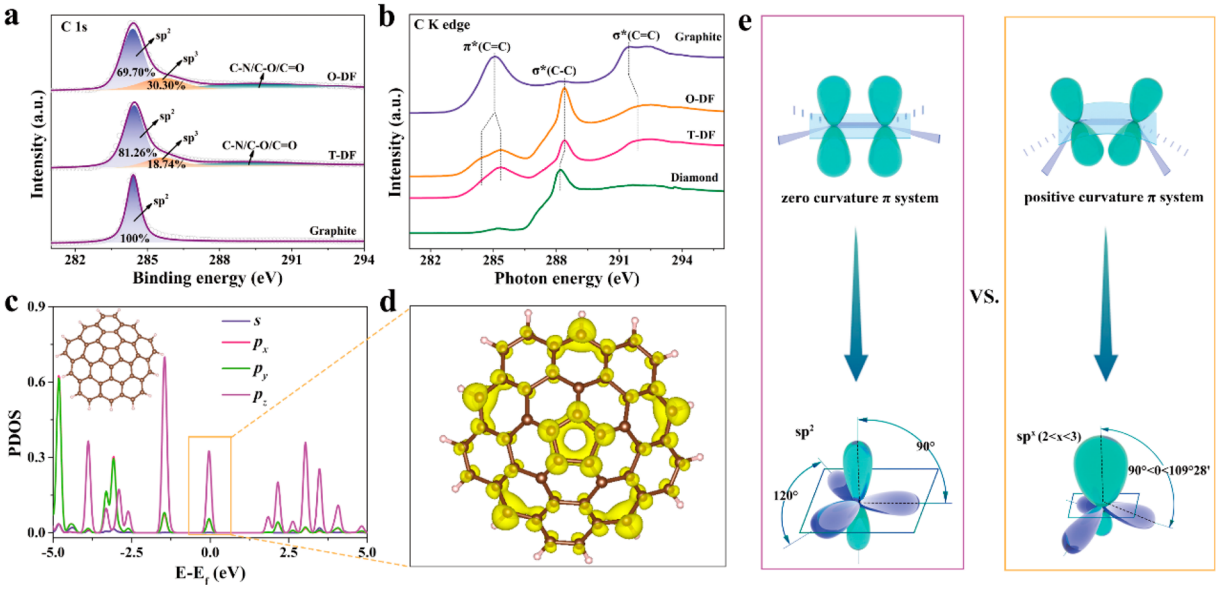

Figure 3. (a) High-resolution XPS C 1s spectra of O-DF, T-DF, and graphite. (b) C K-edge XANES spectra of O-DF, T-DF, graphite, and diamond. (c) PDOS of C atoms for positive curvature structure. (d) Charge density distribution with isosurface values of 0.005 e/Å^3 corresponding to energy windows of positive curvature carbon in (c) near the Fermi level. The yellow represents electron accumulation. (e) Schematic illustration of sp^2-hybridized orbital in a zero curvature system versus sp^x-hybridized orbital in a positive curvature system.

different curvature structures among the planar surface, Riemann surface, and Lobachevskian surface were future characterized. The high-resolution XPS C 1s spectrum of either O-DF or T-DF is fitted with three peaks at around 284.4, 285.6, and 289.2 eV, which are correlated to sp^2-hybridized carbon, sp^3-hybridized carbon, and C−N/C−O/C═O, respectively,[28] suggesting that both O-DF and T-DF exhibit the presence of intrinsic carbon defects in the carbon networks, as compared with sp^2-hybridized graphite (Figure 3a). With the corresponding decrease of sp^2-hybridized content, the sp^3-hybridized content of T-DF and O-DF significantly increases to 18.74% and 30.30%, respectively. This result confirms that the non-coplanar Riemannian surface and non-Euclidean surface originate from the introduction of sp^3-hybridized content, where the absolute values of the curvature are positively correlated with the ratios of sp^3-hybridized content, identifying that the Riemannian surface of O-DF possesses an outstanding curve effect as compared with the non-Euclidean surface of T-DF.

More precisely, the C K-edge X-ray absorption near-edge structure (XANES) spectra reflect the electronic transitions from the C 1s core state into unoccupied σ^* or π^* states above the Fermi level and thereby allow one to distinguish the hybridized orbital types of carbon defects in the Riemannian surface and non-Euclidean geometrical surface.[37−39] For comparison, graphite that serves as a typical representative of sp^2 configuration exhibits two absorption edges located at 285 eV (1s → π^* extractions) and 291.4 eV (1s → σ^* extractions), which are attributed to the π^* and σ^* states of C═C bonds, respectively, while a diamond with only the unique sp^3-hybridized carbons lacks π^* states and is located at 288.2 eV (1s → σ^* transitions), which is assigned to σ^* states of C−C bonds.[37,39] It is clear that the similar peaks of both sp^2 and sp^3 features coexist in the XANES spectra of either O-DF or T-DF (Figure 3b). For instance, the corresponding peaks from the σ^* states of C═C and C−C bonds for O-DF are shifted to 288.4 and 292 eV, respectively. In addition, as compared with graphite, the peak from σ^* states of C−C for O-DF become stronger than that of C═C, indicating an increase in the ratio of sp^3 to sp^2 contents,[39] which is consistent with the XPS results. Similar features are also discovered in the C K-edge XANES spectrum of T-DF. Interestingly, the peak from π^* states of C═C bonds for O-DF is divided into two peaks located at 284.4 and 285.3 eV, one toward lower energy and the other toward higher energy, which implies that the charge transfer occurs among the different carbon atoms, resulting in the local charge-enriched and dispersive charges of the counterparts.[38,39] So far, these results could be closely associated with the change of hybridized orbital types and electronic structure for carbon intrinsic defects in the curved surfaces.

To further discern the distinction of the hybridized orbital form and the electronic structure among the Riemannian surface, planar surface, and Lobachevskian surface, we first studied the projected density of states (PDOS) for zero, positive, and negative curvature graphene. As shown in Figure 3c and Figure S13a, owing to the isotropy and special ring structure, the contributions of the p_x and p_y orbitals for different curvature graphene completely coincide. As is well-known, for perfect graphene with a zero curvature structure, which is entirely composed of coplanar sp^2-hybridized carbon, there is no overlap near the Fermi level between $p_{x/y}$ and p_z orbitals (Figure S13c). For either a positive or negative curvature structure, however, not only does it inherit the tridentate coordination of the coplanar sp^2 hybridization, but also the p_z orbital participates in the hybridization to form the analogous non-coplanar sp^3 hybridization. Normally, the equivalent contributions of p_x, p_y, and p_z orbitals construct the complete sp^3 hybridization. However, the contribution of the p_z orbital in the curved structure is significantly smaller than that of p_x and p_y, indicating that the hybridized type of carbon atoms may be more like the transition state between the conventional sp^2 and sp^3 for the curved defect sites. Subsequently, the theoretical calculations confirm that carbon

https://doi.org/10.1021/acscentsci.2c00411
ACS Cent. Sci. XXXX, XXX, XXX−XXX

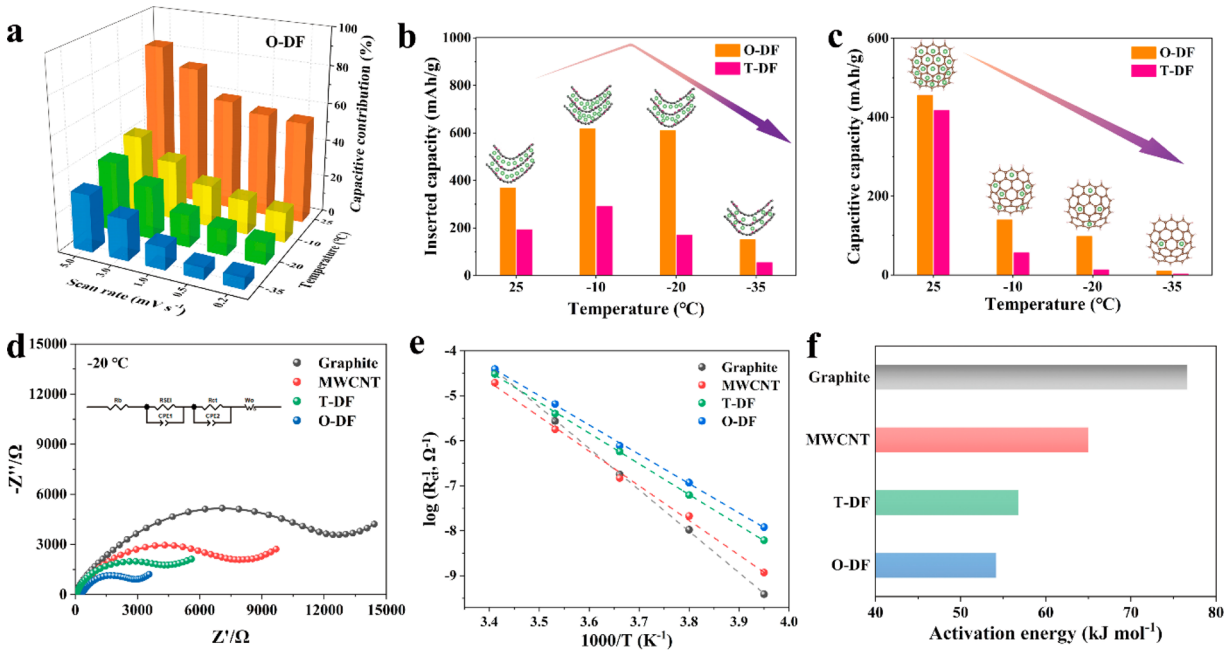

Figure 4. (a) Capacitive contribution ratios of O-DF along with different scan rates and temperatures. (b, c) Diffusion-controlled capacity and surface-controlled capacity of different temperatures for O-DF and T-DF at 0.2 mV s^{-1}. (c–f) Electrochemical impedance spectroscopy (EIS) at −20 °C (d), the simulated Arrhenius plot of charge-transfer resistance (e) and activation energy (f) of the charge-transfer process of O-DF, T-DF, MWCNT, and graphite.

atoms among the pentagonal defects embedded into the Riemann surface tend to adopt new-typed sp^x ($2 < x < 3$) hybridization (Figure S13d), henceforth, referred to as the Riemannian orbital. More importantly, the non-coplanar sp^x hybridization of coordination-unsaturated carbon atoms in the curved carbon would effectively tune the electronic structure. The corresponding charge density distributions of different curvature structures around the Fermi level further prove this conjecture. As shown in Figure 3d and Figure S13b, for the curved structure, the distribution of electrons near the Fermi level of non-hexagonal defect sites is greater than that of the adjacent hexagonal rings. These electrons occupy the p_z orbitals of the bowl-shaped outside at the non-hexagonal defect sites, leading to locally accumulated charges, rather than a conjugated π-system in a zero curvature structure. These theoretical calculations are in close agreement with the XPS and XANES results.

In brief, the Riemannian surface and Lobachevskian surface originate from non-coplanar sp^x hybridized orbitals (Figure 3e), resulting in enriched charges around the Fermi level of non-hexagonal defect sites, which are prone to donate electrons to the corresponding acceptor. The accumulated charges in the positive curvature structure stand out against the corresponding negative curvature structure, resulting from a larger curvature of the Riemannian surface than that of the Lobachevskian surface. In consideration of the high capacity of O-DF at low temperature, it can be inferred that the accumulated charges in the Riemannian surface play a vital role to reduce the activation energy of charge transfer in the low-temperature Li-ion storage process.

To explore the mechanism of Li-ion storage, an electrochemical kinetics test was employed. Figure S14 shows the CV curves of O-DF for different temperatures along with different scan rates ranging from 0.2 to 5.0 mV s^{-1}. The total capacity is quantitatively divided into the diffusion-controlled contribution and surface-induced capacitive contribution according to the mechanism of Li-ion storage, as detailed analysis in Supporting Information. In this case, the surface-induced capacitive contribution continuously increases with the increase of the scan rate at the same temperature as well as dramatically decreases with a drop in the operating temperature at the same scan rate (Figure 4a). For instance, when the ambient temperature is decreased from 25 °C to −35 °C, the corresponding capacitive contribution is reduced from 59.5% to 11.9% at a fixed scan rate of 1.0 mV s^{-1} (Figure S15). It is clear that the diffusion-controlled behavior dominates the total charge-storage capacity at low temperature instead of the mixed mechanism for Li-ion storage at room temperature.

Moreover, the specific capacity of O-DF at 0.1 A g^{-1} is nearly equal to that for the CV measured data at 0.2 mV s^{-1}. As a consequence, the diffusion-controlled capacity and surface-controlled capacity at different temperatures were separated from the CV results, respectively.[40] Concretely, the diffusion-controlled capacity of O-DF increases at first and later decreases as the temperature, reaching a peak at −10 °C, where this attenuation trend is inconsistent with that of the total capacity (Figure 4b). This result could be ascribed to the screen effect of the saturated adsorption of solvated Li^+ on the Riemannian surface at room temperature and the stimulative effect of the unsaturated adsorption of solvated Li^+ at low temperature. In other words, the excessive Li^+ adsorbed on the Riemannian surface at room temperature prevents solvated Li^+ from reaching the liquid–solid interface due to the Li^+ Coulombic repulsion, but when the temperature decreases, some adsorption sites with a relatively low activity such as the coplanar sp^2 carbon atoms switch to the chemically inert sites, or rather sp^2-hybridized carbon atoms binding to solvated Li^+ are insufficient to break the coordinate interaction between the organic solvent and Li^+ and split the solvation sheath structures for Li-ion storage. On the other hand, the limited layer

https://doi.org/10.1021/acscentsci.2c00411
ACS Cent. Sci. XXXX, XXX, XXX−XXX

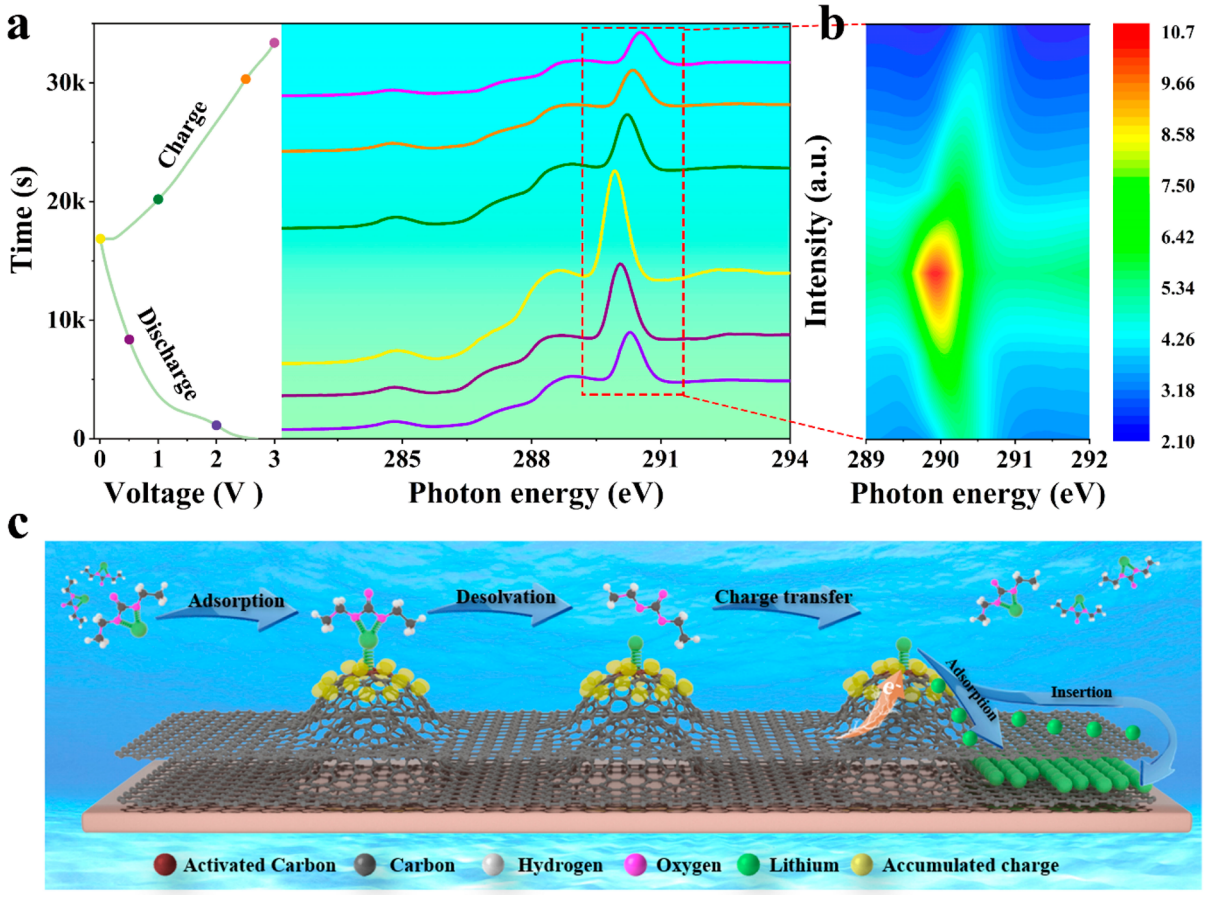

Figure 5. (a) Ex-situ C K-edge XANES spectra of O-DF at different charge−discharge states of −20 °C. (b) Detailed view of a C K-edge XANES contour plot of the Li−C band at the corresponding charge/discharge states in (a). (c) Accumulated charges originate from the sp^2/sp^3-hybridized orbital of the positive curvature structure for low-temperature lithium storage.

spacings in graphite prohibit the intercalated storage of solvated Li^+. This contradiction means that, therefore, the extensive loss of the diffusion-controlled capacity at low temperature is mainly due to the lack of activated adsorption sites for Li^+ desolvation. This speculation coincidentally coincides with the fact that the surface-controlled capacity of O-DF is remarkably reduced with the decrease of temperature (Figure 4c). Consistently, similar trends are also found in the electrochemical kinetics tests of the T-DF electrode (Figures S16−18). In particular, the surface-controlled capacity of O-DF is much higher than that of T-DF at each operating temperature (Figure 4c), meaning that more localized charges in the Riemannian surface should activate the pentagonal defects as highly active adsorption sites to reduce the energy barrier of charge transfer for the sluggish Li^+ desolvation process in an extremely cold environment.

As a rule, the true limitation of low-temperature performance is substantially due to the interfacial process, typically, substantially increased charge-transfer resistance (R_{ct}).[4,9] The change of charge-transfer resistance with temperature is largely determined by the activation energy (E_a).[4] To verify that the energy barrier of charge transfer in the Riemannian surface is lower than that of other surfaces at low temperature, electrochemical impedance spectroscopy (EIS) of O−DT, T-DF, MWCNT, and graphite anodes were collected at various temperatures (Figure S19). For these four anodes, the charge-transfer resistance significantly increases with the decrease of temperature (Table S2). Especially, the charge-transfer resistance of O-DF is far less than that of other anodes at −20 °C (Figure 4d). According to the Arrhenius plot between R_{ct} and E_a for different anodes (Figure 4e, detailed calculations in Supporting Information), the value E_a of charge-transfer resistance in O-DF (54.2 kJ/mol) is much lower than that of other electrodes (56.8, 76.6, and 65.0 kJ/mol for T-DF, MWCNT, and graphite, respectively) (Figure 4f). This result means that the facilitated Li^+ transport across the electrolyte/electrode interface should be attributed to the introduction of Riemannian surface, which alters the charge transfer between solvated Li^+ and surface carbon atoms for Li^+ desolvation in an extremely cold environment.

To further confirm that the charge transfer between the pentagonal defect sites and solvated Li^+ occurs on the Riemannian surface, XANES spectra were collected by the surface-sensitive total electron yield method with a probing depth of ∼5 nm to monitor the change of chemical bonds on the Riemannian surface during the charge−discharge process at −20 °C.[38] After being discharged to 0.01 V, it is clear that the C K-edge XANES spectrum of O-DF shows that the intensity from π^* states of the C=C bonds and σ^*states of C−C bonds dramatically decreases relative to that of bare O-DF (Figure S20a). Meanwhile, a new peak located at 289.9 eV is shifted to high energy compared to the corresponding σ^*states of C−C bonds, which stems from the C 1 s core level to σ^* transitions of Li−C bonds.[38,41] Also, the positive curvature structure of O-DF was maintained after 100 cycles at −20 °C (Figure S20b). These results indicate that solvated Li^+

https://doi.org/10.1021/acscentsci.2c00411
ACS Cent. Sci. XXXX, XXX, XXX−XXX

is first adsorbed on the Riemannian surface, and then some charges transfer from carbon atoms to the solvated Li^+, resulting in Li^+ desolvation at the liquid−solid interface to form the Li−C coordinate bonds.

Furthermore, ex-situ C K-edge XANES spectra of O-DF were obtained at different charge−discharge depths of −20 °C. As shown in Figure 5a,b, when the discharged depths increase from 2.0 to 0.01 V, the intensity from σ^* states of Li−C bonds increases because of a large number of solvated Li^+ adsorbed on the different Li-ion storage sites. More importantly, the corresponding peak position continuously shifts toward a lower energy, suggesting that the solvated Li^+ prefers to be adsorbed on the charge-enriched pentagonal defects that serve as efficient active sites at low temperature, which strongly depends on more charge transfer from the carbon intrinsic defects to solvated Li^+ than that of the subsequent adsorption at low active sites. The strengthened solvated Li^+ binding to the charge-enriched sites would decrease the activation energy of charge transfer at the liquid−solid interface and allow dissociation of the coordinate bonds between the organic solvent and Li^+ to execute the diffusion-controlled Li^+ insertion storage even at −35 °C. In contrast, during the charge process, the peak position reversibly shifts back to high energy together with a decrease in peak intensity, again indicating the excellent low-temperature cycling stability.

As shown in Figure 5c, non-coplanar Riemannian orbitals with unsaturated coordination could effectively adjust the electronic rearrangement around the pentagonal defect sites for Li^+ desolvation at low temperature, resulting in locally accumulated charges of the intrinsic defect sites. Under the orientated guidance of the reinforced electrostatic attraction induced by the enriched charges, the solvated Li^+ as the electrophilic species is expected to be adsorbed at the pentagonal defect sites. Subsequently, the sp^x-hybridized orbitals donate more negative charges to the adsorbed Li^+, leading to the formation of stronger Li−C coordinate interactions between solvated Li^+ and the adsorption sites as compared with that of solvated Li^+ itself. The strengthened solvated Li^+ binding to the charge-enriched sites makes it possible for Li^+ desolvation to break the coordinate bonds between Li^+ and organic solvent even at subambient temperatures. Eventually, the enriched charges in the non-coplanar Riemannian surface could effectively enhance the charge transfer from the sp^{-x}-hybridized carbon to solvated Li^+ and reinforce the coordinate ability of intrinsic defect sites for Li^+ desolvation. It supports more Li^+ adsorption and insertion in an extremely cold environment, which accounts for the low-temperature, high reversible capacity of O-DF.

CONCLUSIONS

In summary, we demonstrate that the Riemannian surface could manipulate the hybridized orbital types of carbon atoms for surface electronic modulation and thus reinforce the coordinate interaction between the solvated Li^+ and adsorption sites as an effective strategy to address severe capacity degradation in an extremely cold environment. Inspired by this, we synthesized a high capacity O-DF carbon-based anode material for low-temperature LIBs through direct low-temperature pyrolysis of ZIF-67, which possesses a non-coplanar Riemannian surface with a positive curvature structure. When the temperature declines to −20 °C, the as-prepared O-DF exhibits a high reversible capacity of 624 mAh g^{-1} with an 85.9% capacity retention at 0.1 A g^{-1}, far surpassing the counterpart with either zero or negative curvature. Even if the temperature drops to −35 °C, the reversible capacity is still effectively retained at 160 mAh g^{-1} after 200 cycles. Various characterizations and theoretical calculations demonstrate that the Riemannian surface induces non-coplanar sp^x-hybridized orbitals with unsaturated coordination, where the locally accumulated charges reduce the energy barrier of charge transfer in the Li^+ desolvation process. Ex-situ C K-edge XANES spectra further confirm that these enriched charges of sp^x-hybridized orbitals activate pentagonal defects as high-activity adsorption sites and donate more negative charge to the solvated Li^+ adsorbed on the surface, thus forming stronger Li−C coordinate bonds for Li^+ desolvation in an extremely cold environment.

ASSOCIATED CONTENT

Supporting Information

The Supporting Information is available free of charge at https://pubs.acs.org/doi/10.1021/acscentsci.2c00411.

Experimental details, theoretical calculations, characterization data, and electrochemical performance data (PDF)

AUTHOR INFORMATION

Corresponding Authors

Xi Wang − *Department of Physics, School of Physical Science and Engineering, Beijing Jiaotong University, Beijing 100044, China*; orcid.org/0000-0003-3910-9575; Email: xiwang@bjtu.edu.cn

Jiannian Yao − *Key Laboratory of Photochemistry, Beijing National Laboratory for Molecular Sciences, Institute of Chemistry, Chinese Academy of Sciences, Beijing 100190, China*; Email: jnyao@iccas.ac.cn

Authors

Zongjing Lu − *School of Chemical Engineering and Technology, Tianjin University, Tianjin 300072, China*

Jingnan Wang − *Molecular Plus, Tianjin University, Tianjin 300072, China*

Xuechun Cheng − *Molecular Plus, Tianjin University, Tianjin 300072, China*

Weiwei Xie − *Institute of Physical Chemistry, Karlsruhe Institute of Technology, Karlsruhe 76131, Germany*

Zhiyi Gao − *School of Chemical Engineering and Technology, Tianjin University, Tianjin 300072, China*

Xuejing Zhang − *School of Chemical Engineering and Technology, Tianjin University, Tianjin 300072, China*

Yong Xu − *Innovation Laboratory for Sciences and Technologies of Energy Materials of Fujian Province (IKKEM), Xiamen 361005, China*

Ding Yi − *Department of Physics, School of Science, Beijing Jiaotong University, Beijing 100044, China*; orcid.org/0000-0001-9294-8760

Yijun Yang − *Department of Physics, School of Science, Beijing Jiaotong University, Beijing 100044, China*; orcid.org/0000-0002-9243-6228

Complete contact information is available at: https://pubs.acs.org/10.1021/acscentsci.2c00411

Author Contributions

#Z.L., J.W. and X.C. contributed equally to this work.

https://doi.org/10.1021/acscentsci.2c00411
ACS Cent. Sci. XXXX, XXX, XXX−XXX

Notes

The authors declare no competing financial interest.

■ ACKNOWLEDGMENTS

This work was supported financially by "Key Program for International S&T Cooperation Projects of China" from the Ministry of Science and Technology of China (Grant No. 2018YFE0124600). This work was also supported financially by the National Natural Science Foundation of China (Grant Nos. 91961125, 21905019, and 51802013), Science and Technology Project of Guangdong Province (Grant No. 2020B0101370001), and the Chemistry and Chemical Engineering Guangdong Laboratory (Grant No. 1932004). We thank the beamlines 4B7B at Beijing Synchrotron Radiation Facility (BSRF).

■ REFERENCES

(1) Dong, X.; Guo, Z.; Guo, Z.; Wang, Y.; Xia, Y. Organic Batteries Operated at −70 °C. *Joule* **2018**, *2* (5), 902.

(2) Fan, X.; Ji, X.; Chen, L.; Chen, J.; Deng, T.; Han, F.; Yue, J.; Piao, N.; Wang, R.; Zhou, X.; Xiao, X.; Chen, L.; Wang, C. All-Temperature Batteries Enabled by Fluorinated Electrolytes with Non-Polar Solvents. *Nat. Energy* **2019**, *4* (10), 882.

(3) Holoubek, J.; Liu, H.; Wu, Z.; Yin, Y.; Xing, X.; Cai, G.; Yu, S.; Zhou, H.; Pascal, T. A.; Chen, Z.; Liu, P. Tailoring Electrolyte Solvation for Li Metal Batteries Cycled at Ultra-Low Temperature. *Nat. Energy* **2021**, *6* (3), 303.

(4) Zhang, W.; Sun, X.; Tang, Y.; Xia, H.; Zeng, Y.; Qiao, L.; Zhu, Z.; Lv, Z.; Zhang, Y.; Ge, X.; Xi, S.; Wang, Z.; Du, Y.; Chen, X. Lowering Charge Transfer Barrier of $LiMn_2O_4$ via Nickel Surface Doping to Enhance Li^+ Intercalation Kinetics at Subzero Temperatures. *J. Am. Chem. Soc.* **2019**, *141* (36), 14038.

(5) Lu, J.; Wang, C.; Yu, H.; Gong, S.; Xia, G.; Jiang, P.; Xu, P.; Yang, K.; Chen, Q. Oxygen/Fluorine Dual-Doped Porous Carbon Nanopolyhedra Enabled Ultrafast and Highly Stable Potassium Storage. *Adv. Funct. Mater.* **2019**, *29* (49), 1906126.

(6) Wang, C. Y.; Zhang, G.; Ge, S.; Xu, T.; Ji, Y.; Yang, X. G.; Leng, Y. Lithium-Ion Battery Structure that Self-Heats at Low Temperatures. *Nature* **2016**, *529* (7587), 515.

(7) Smart, M. C.; Ratnakumar, B. V.; Whitcanack, L. D.; Chin, K. B.; Surampudi, S.; Croft, H.; Tice, D.; Staniewicz, R. Improved Low-Temperature Performance of Lithium-Ion Cells with Quaternary Carbonate-Based Electrolytes. *J. Power Sources* **2003**, *119*, 349.

(8) Rustomji, C. S.; Yang, Y.; Kim, T. K.; Mac, J.; Kim, Y. J.; Caldwell, E.; Chung, H.; Meng, Y. S. Liquefied Gas Electrolytes for Electrochemical Energy Storage Devices *Science* **2017**, *356* (6345). DOI: 10.1126/science.aal4263

(9) Que, L.; Yu, F.; Xia, Y.; Deng, L.; Goh, K.; Liu, C.; Jiang, Y.; Sui, X.; Wang, Z. Enhancing Na-Ion Storage at Subzero Temperature via Interlayer Confinement of Sn^{2+}. *ACS Nano* **2020**, *14* (10), 13765.

(10) Varzi, A.; Mattarozzi, L.; Cattarin, S.; Guerriero, P.; Passerini, S. 3D Porous Cu-Zn Alloys as Alternative Anode Materials for Li-Ion Batteries with Superior Low T Performance. *Adv. Energy Mater.* **2018**, *8* (1), 1701706.

(11) Sun, Z.; Li, Z.; Gao, L.; Zhao, X.; Han, D.; Gan, S.; Guo, S.; Niu, L. Grafting Benzenediazonium Tetrafluoroborate onto $Li-Ni_xCo_yMn_zO_2$ Materials Achieves Subzero-Temperature High-Capacity Lithium-Ion Storage via a Diazonium Soft-Chemistry Method. *Adv. Energy Mater.* **2019**, *9* (6), 1802946.

(12) Li, Q.; Lu, D.; Zheng, J.; Jiao, S.; Luo, L.; Wang, C. M.; Xu, K.; Zhang, J. G.; Xu, W. Li^+-Desolvation Dictating Lithium-Ion Battery's Low-Temperature Performances. *ACS Appl. Mater. Interfaces* **2017**, *9* (49), 42761.

(13) Jiang, L.; Dong, D.; Lu, Y. Design Strategies for Low Temperature Aqueous Electrolytes *Nano Res. Energy* **2022**. DOI: 10.26599/NRE.2022.9120003

(14) Holoubek, J.; Yin, Y.; Li, M.; Yu, M.; Meng, Y. S.; Liu, P.; Chen, Z. Exploiting Mechanistic Solvation Kinetics for Dual-Graphite Batteries with High Power Output at Extremely Low Temperature. *Angew. Chem. Int. Ed* **2019**, *58* (52), 18892.

(15) Xu, K.; von Cresce, A.; Lee, U. Differentiating Contributions to "Ion Transfer" Barrier from Interphasial Resistance and Li^+ Desolvation at Electrolyte/Graphite Interface. *Langmuir* **2010**, *26* (13), 11538.

(16) Liu, Y.; Yang, B.; Dong, X.; Wang, Y.; Xia, Y. A Simple Prelithiation Strategy to Build a High-Rate and Long-Life Lithium-Ion Battery with Improved Low-Temperature Performance. *Angew. Chem. Int. Ed* **2017**, *56* (52), 16606.

(17) Gupta, A.; Manthiram, A. Designing Advanced Lithium-Based Batteries for Low-Temperature Conditions. *Adv. Energy Mater.* **2020**, *10* (38), 2001972.

(18) Liu, X.; Wang, Y.; Yang, Y.; Lv, W.; Lian, G.; Golberg, D.; Wang, X.; Zhao, X.; Ding, Y. A MoS_2/Carbon Hybrid Anode for High-Performance Li-Ion Batteries at Low Temperature. *Nano Energy* **2020**, *70*, 104550.

(19) Hou, J.; Yang, M.; Wang, D.; Zhang, J. Fundamentals and Challenges of Lithium Ion Batteries at Temperatures between − 40 and 60 °C. *Adv. Energy Mater.* **2020**, *10* (18), 1904152.

(20) Zhang, D. B.; Akatyeva, E.; Dumitrica, T. Bending Ultrathin Graphene at the Margins of Continuum Mechanics. *Phys. Rev. Lett.* **2011**, *106* (25), 255503.

(21) Lu, Z.; Gao, D.; Yi, D.; Yang, Y.; Wang, X.; Yao, J. sp^2/sp^3 Hybridized Carbon as an Anode with Extra Li-Ion Storage Capacity: Construction and Origin. *ACS Cent. Sci.* **2020**, *6* (8), 1451.

(22) Zhang, Y.; Zhu, Y.; Lan, D.; Pun, S. H.; Zhou, Z.; Wei, Z.; Wang, Y.; Lee, H. K.; Lin, C.; Wang, J.; Petrukhina, M. A.; Li, Q.; Miao, Q. Charging a Negatively Curved Nanographene and Its Covalent Network. *J. Am. Chem. Soc.* **2021**, *143* (13), 5231.

(23) Urgel, J. I.; Di Giovannantonio, M.; Segawa, Y.; Ruffieux, P.; Scott, L. T.; Pignedoli, C. A.; Itami, K.; Fasel, R. Negatively Curved Warped Nanographene Self-Assembled on Metal Surfaces. *J. Am. Chem. Soc.* **2019**, *141* (33), 13158.

(24) Fernandez-Garcia, J. M.; Evans, P. J.; Medina Rivero, S.; Fernandez, I.; Garcia-Fresnadillo, D.; Perles, J.; Casado, J.; Martin, N. π-Extended Corannulene-Based Nanographenes: Selective Formation of Negative Curvature. *J. Am. Chem. Soc.* **2018**, *140* (49), 17188.

(25) Li, C.; Zhang, X.; Cao, Z. Triangular and Fibonacci Number Patterns Driven by Stress on Core/Shell Microstructures. *Science* **2005**, *309* (5736), 909.

(26) Zhou, H.; Zheng, M.; Tang, H.; Xu, B.; Tang, Y.; Pang, H. Amorphous Intermediate Derivative from ZIF-67 and Its Outstanding Electrocatalytic Activity. *Small* **2020**, *16* (2), 1904252.

(27) Toh, C. T.; Zhang, H.; Lin, J.; Mayorov, A. S.; Wang, Y. P.; Orofeo, C. M.; Ferry, D. B.; Andersen, H.; Kakenov, N.; Guo, Z.; Abidi, I. H.; Sims, H.; Suenaga, K.; Pantelides, S. T.; Ozyilmaz, B. Synthesis and Properties of Free-Standing Monolayer Amorphous Carbon. *Nature* **2020**, *577* (7789), 199.

(28) Wang, R.; Yang, J.; Chen, X.; Zhao, Y.; Zhao, W.; Qian, G.; Li, S.; Xiao, Y.; Chen, H.; Ye, Y.; Zhou, G.; Pan, F. Highly Dispersed Cobalt Clusters in Nitrogen-Doped Porous Carbon Enable Multiple Effects for High-Performance Li−S Battery. *Adv. Energy Mater.* **2020**, *10* (9), 1903550.

(29) Klein, Y.; Efrati, E.; Sharon, E. Shaping of Elastic Sheets by Prescription of Non-Euclidean Metrics. *Science* **2007**, *315*, 1116.

(30) Romo-Herrera, J. M.; Sumpter, B. G.; Cullen, D. A.; Terrones, H.; Cruz-Silva, E.; Smith, D. J.; Meunier, V.; Terrones, M. An Atomistic Branching Mechanism for Carbon Nanotubes: Sulfur as the Triggering Agent. *Angew. Chem. Int. Ed* **2008**, *120* (16), 2990.

(31) Pun, S. H.; Miao, Q. Toward Negatively Curved Carbons. *Acc. Chem. Res.* **2018**, *51* (7), 1630.

(32) Liu, W.; Zhao, L.; Zurek, E.; Xia, J.; Zheng, Y. H.; Lin, H. Q.; Liu, J. Y.; Miao, M. S. Building Egg-Tray-Shaped Graphenes that Have Superior Mechanical Strength and Band Gap. *Npj Comput. Mater.* **2019**, *5* (1), 1.

https://doi.org/10.1021/acscentsci.2c00411
ACS Cent. Sci. XXXX, XXX, XXX−XXX

(33) Xia, B. Y.; Yan, Y.; Li, N.; Wu, H. B.; Lou, X. W.; Wang, X. A Metal−Organic Framework-Derived Bifunctional Oxygen Electrocatalyst *Nat. Energy* **2016**, *1* (1). DOI: 10.1038/nenergy.2015.6
(34) Xu, Y.; Zhang, C.; Zhou, M.; Fu, Q.; Zhao, C.; Wu, M.; Lei, Y. Highly Nitrogen Doped Carbon Nanofibers with Superior Rate Capability and Cyclability for Potassium Ion Batteries. *Nat. Commun.* **2018**, *9* (1), 1720.
(35) Zheng, F.; Yang, Y.; Chen, Q. High Lithium Anodic Performance of Highly Nitrogen-Doped Porous Carbon Prepared from a Metal-Organic Framework. *Nat. Commun.* **2014**, *5* (1), 1.
(36) Wang, L.; Wang, Z.; Xie, L.; Zhu, L.; Cao, X. ZIF-67-Derived N-Doped Co/C Nanocubes as High-Performance Anode Materials for Lithium-Ion Batteries. *ACS Appl. Mater. Interfaces* **2019**, *11* (18), 16619.
(37) Osswald, S.; Yushin, G.; Mochalin, V.; Kucheyev, S. O.; Gogotsi, Y. Control of sp^2/sp^3 Carbon Ratio and Surface Chemistry of Nanodiamond Powders by Selective Oxidation in Air. *J. Am. Chem. Soc.* **2006**, *128* (35), 11635.
(38) Zhang, L.; Li, X.; Augustsson, A.; Lee, C. M.; Rubensson, J. E.; Nordgren, J.; Ross, P. N.; Guo, J. H. Revealing the Electronic Structure of LiC_6 by Soft X-Ray Spectroscopy. *Appl. Phys. Lett.* **2017**, *110* (10), 104106.
(39) Lee, D. W.; Seo, J. W. sp^2/sp^3 Carbon Ratio in Graphite Oxide with Different Preparation Times. *J. Phys. Chem. C* **2011**, *115* (6), 2705.
(40) Zhai, T.; Sun, S.; Liu, X.; Liang, C.; Wang, G.; Xia, H. Achieving Insertion-Like Capacity at Ultrahigh Rate via Tunable Surface Pseudocapacitance. *Adv. Mater.* **2018**, *30* (12), 1706640.
(41) Langer, J.; Epp, V.; Heitjans, P.; Mautner, F. A.; Wilkening, M. Lithium Motion in the Anode Material LiC_6 as Seen via Time-Domain ^7Li NMR. *Phys. Rev. B* **2013**, *88* (9), 094304.

https://doi.org/10.1021/acscentsci.2c00411
ACS Cent. Sci. XXXX, XXX, XXX−XXX